



Optics Letters

Inverse design of a polarization demultiplexer for on-chip path-entangled photon-pair sources based on single quantum dots

EMERSON G. MELO,^{1,2}  WILLIAM ESHBAUGH,³ EDWARD B. FLAGG,³  AND MARCELO DAVANCO^{2,*} 

¹Materials Engineering Department, Lorena School of Engineering, University of São Paulo, Lorena, SP 12602-810, Brazil

²National Institute of Standards and Technology, Gaithersburg, Maryland, 20899, USA

³Department of Physics and Astronomy, West Virginia University, Morgantown, West Virginia, 26506, USA

*marcelo.davanco@nist.gov

Received 23 May 2023; revised 3 August 2023; accepted 3 August 2023; posted 7 August 2023; published 21 August 2023

Epitaxial quantum dots can emit polarization-entangled photon pairs. If orthogonal polarizations are coupled to independent paths, then the photons will be path-entangled. Through inverse design with adjoint method optimization, we design a quantum dot polarization demultiplexer, a nanophotonic geometry that efficiently couples orthogonally polarized transition dipole moments of a single quantum dot to two independent waveguides. We predict 95% coupling efficiency, cross talk less than 0.1%, and Purcell radiative rate enhancement factors over 11.5 for both dipoles, with sensitivity to dipole misalignment and orientation comparable to that of conventional nanophotonic geometries. We anticipate our design will be valuable for the implementation of triggered, high-rate sources of path-entangled photon-pairs on chip. © 2023 Optica Publishing Group

<https://doi.org/10.1364/OL.496129>

Single quantum dots (QDs) are promising sources of polarization-entangled photon pairs [1–3], being capable of triggered emission at fast rates, with inherently sub-Poissonian statistics and high indistinguishability [4–6]. Such characteristics indicate potential for superior performance compared with that of spontaneous parametric sources, which are fundamentally limited in brightness by their Poissonian statistics [4].

Polarization-entangled photon pairs can be emitted by a QD during the decay cascade from the biexciton state through the neutral exciton to the ground state [7–10]. To produce a bright entangled photon source from a single QD, the two spectrally distinct photons from the cascade must be funneled into desirable collection channels without any polarization filtering so as to preserve the entanglement. Control of the spontaneous decay rates of the transitions is likely also necessary to maximize photon indistinguishability and the fidelity of entanglement [3,11]. A variety of photonic nanostructures have been used to efficiently extract photon pairs from QDs and enable efficient collection into free-space optics, including solid immersion lenses (SILs) [10], micropillars [12], nanowires [13], and

nanophotonic cavities [1,2,5]. Photonic nanostructures have also been used to couple single-photon emission into integrated photonic waveguides [6,14,15]. Direct coupling of entangled photon pairs into integrated photonic waveguides is highly desirable, as it would allow quantum state manipulation and measurement in compact, stable, and potentially fast photonic integrated circuits [16]. Jin *et al.* [17] have recently demonstrated coupling of QD-emitted entangled photon pairs to two orthogonal modes of a single multimode waveguide. Such a scheme has limited design freedom, preventing uniform coupling efficiency for each waveguide mode and making Purcell enhancement of the radiative rate highly challenging, if not impossible.

In the present work, we employ electromagnetic inverse design [18] to optimize a simulated polarization demultiplexer, a nanophotonic structure that will efficiently couple orthogonally polarized photons emitted by a QD into separate on-chip waveguides. While polarization-entangled photon pairs emitted by the biexciton cascade are usually coupled to the same free-space path, the geometry we propose will guide the two polarizations into distinct waveguides within the on-chip device. This is expected to produce photon pairs that are entangled in the waveguide path degree of freedom rather than in polarization. Our device design is furthermore predicted to provide a Purcell radiative rate enhancement for both biexciton and exciton transitions, which is desirable for photon indistinguishability and entanglement fidelity control [3,11]. Purcell enhancement can also be leveraged for enhancing source efficiency, since it enhances dipole coupling probability to a single confined spatial mode, which can then couple to an output waveguide [19]. The optimized simulated design exhibits a coupling efficiency of 95%, with a cross talk of less than 0.1% and a Purcell factor over 11.5.

Entangled photon emission from a single QD relies on the energy structure shown in the inset of Fig. 1. The QD supports exciton (X) and biexciton (XX) states, in which one or two electron-hole pairs are confined within the QD. The single exciton is typically split into two states, X_V and X_H , separated in energy by the fine-structure splitting, E_{FSS} [20]. Cascaded spontaneous decay from XX to X, then from X to the ground state (G), results

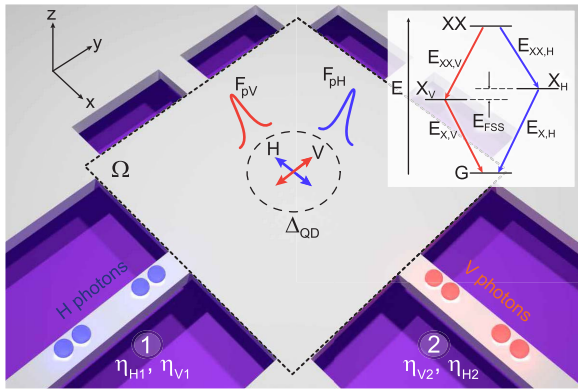


Fig. 1. Schematic of the geometry optimization problem in a suspended AlGaAs slab. QD transitions with horizontal (H, blue) or vertical (V, red) dipole moments are to be coupled into output waveguides 1 and 2, with maximized efficiencies η_{H1} and η_{V2} and minimized cross talks η_{H2} and η_{V1} . The domain Ω is the starting geometry for optimization. Inset shows QD energy levels and biexciton-exciton-ground (XX-X-G) transitions. Blue and red arrows indicate H- or V-polarized dipole moment transitions, respectively.

in a pair of sequentially emitted, spectrally distinct photons with identical linear polarizations, vertical (V) or horizontal (H). The cascade follows either the red or blue decay paths depicted in the inset of Fig. 1, so both photons are H-polarized or both are V-polarized. The photons' polarizations are thus *correlated* in the H/V basis, but the spectral distinguishability caused by the non-zero E_{FSS} provides “which path” information that precludes polarization *entanglement* [9,21]. If $E_{\text{FSS}} = 0$, however, then both XX-X transitions are degenerate and both X-G transitions are degenerate. This eliminates the spectral “which path” information, producing a photon pair in the maximally entangled Bell state, $(|H_{\text{XX}}, H_{\text{X}}\rangle + |V_{\text{XX}}, V_{\text{X}}\rangle)/\sqrt{2}$, where H/V refer to the polarization and XX/X refer to the energy of the photon [7]. In this state, the photons' polarizations will be correlated in any polarization measurement basis, which is a key characteristic of quantum entanglement. In the H/V basis, the photons' polarizations will always be the same, whereas in the right/left circular basis, their polarizations will always be orthogonal.

As suggested by Fig. 1, in our device, the two orthogonal linear polarizations of the QD transitions are mapped to two separate waveguides. A linearly polarized dipole emits most strongly in the direction perpendicular to its orientation, which we exploit by optimizing the coupling of the H dipole to waveguide 1 and the V dipole to waveguide 2. For a QD with $E_{\text{FSS}} = 0$, the resulting state consists of waveguided photon pairs in the maximally entangled Bell state $(|1_{\text{XX}}, 1_{\text{X}}\rangle + |2_{\text{XX}}, 2_{\text{X}}\rangle)/\sqrt{2}$, where 1 and 2 refer to the output waveguides and subscripts refer to the transition energy. We note that further separating X and XX photons may be necessary to leverage entanglement in applications, which requires a frequency-selective spatial demultiplexer. Whereas, e.g., diffraction gratings can be used for free-space photons [1], various implementations are possible for on-chip photons; e.g., an add-drop filter [22]. We note also that GaAs QDs obtained by local droplet etching have been shown to display near-zero E_{FSS} [3], a central factor in past entangled pair source demonstrations [2], which justifies our choice of material system. For InAs QDs with typically larger E_{FSS} , additional effort must be made to eliminate the splitting, e.g., via strain [23] or the DC [24] or optical [9] Stark effect.

Using electromagnetic inverse design [19,25], we have optimized a nanophotonic geometry that provides the described functionality for a GaAs QD embedded in a 150-nm-thick suspended $\text{Al}_{0.4}\text{Ga}_{0.6}\text{As}$ slab. The starting geometry, depicted in Fig. 1, has a square design region Ω ($3\ \mu\text{m} \times 3\ \mu\text{m}$) with two 300-nm-wide single-mode output waveguides, labeled 1 and 2, along the y- and x-directions. There are additional anchor points at the corners and unused sides of the design region, which would be necessary in a realistic suspended device. The QD was modeled as an x- or y-oriented electric dipole source, corresponding respectively to the H and V transitions. Though biexciton and exciton photons are spectrally distinct, their frequencies typically differ by only 0.1%, so optimizing a single frequency was deemed sufficient. During the optimization process, the starting domain Ω was transformed to provide efficient and highly directional coupling of the H and V dipole emission into the fundamental modes of the output waveguides 1 and 2, respectively.

The optimization was first cast as the multi-objective minimization problem [19]

$$\min_{\rho} F(\mathbf{x}(\boldsymbol{\varepsilon}(\rho))) = (1 - \eta_{H1}(\mathbf{x}))^2 + (1 - \eta_{V2}(\mathbf{x}))^2 + (\eta_{H2}(\mathbf{x}))^2 + (\eta_{V1}(\mathbf{x}))^2 + \left(\frac{1}{F_{pV}^{\theta}} - \frac{1}{F_{pV}(\mathbf{x})}\right)^2 + \left(\frac{1}{F_{pH}^{\theta}} - \frac{1}{F_{pH}(\mathbf{x})}\right)^2. \quad (1)$$

Here, $\mathbf{x} = [\mathbf{E}, \mathbf{H}]^T$ is a vector containing the electromagnetic fields produced by a current dipole source with angular frequency ω in a medium with permittivity $\boldsymbol{\varepsilon}$. The cost function $F(\mathbf{x})$ was defined to maximize the coupling efficiencies, η_{H1} and η_{V2} , and Purcell factors, F_{pV} and F_{pH} , while simultaneously suppressing cross talk quantified by η_{H2} and η_{V1} .

Coupling efficiencies and cross talk are expressed as $\eta_{\phi,n} = (|a_{\phi,n}|^2 P_{\phi,n})/P_0$, where $a_{\phi,n}$ is the complex amplitude coefficient for the fundamental mode in the modal expansion of the outgoing wave in the plane perpendicular to output waveguide n [26]. Here, $P_{\phi,n}$ is the longitudinal component of the Poynting vector for the (non-normalized) fundamental waveguide mode integrated over the waveguide cross section and P_0 is the total power emitted by the source. The index $\phi \in \{V, H\}$ refers to power originating from the vertical (V) or horizontal (H) QD transitions. Radiative rate enhancements for both QD transitions are encouraged by including the Purcell factors of the horizontal (F_{pH}) and vertical (F_{pV}) dipole polarizations, obtained as the ratio $F_{p\phi} = \text{LDOS}_{D,\phi}/\text{LDOS}_{B,\phi}$ between the per-polarization local electromagnetic density of states (LDOS) in the nanophotonic device (D) and in bulk semiconductor (B) [27]. During optimization, the Purcell factors will tend toward the respective target values F_{pH}^{θ} and F_{pV}^{θ} , which are set to infinity in this case. More details about the formulation of the performance metrics within the cost function are in Ref. [19]. The permittivity $\boldsymbol{\varepsilon}(\rho)$ has a spatial dependence described by a set of design parameters $\rho \in [0, 1]$, so $F(\mathbf{x})$ is, ultimately, a function of ρ .

Gradient-based optimization engines require accurate and efficient calculation of the sensitivities $\partial F/\partial \rho$. The adjoint method efficiently calculates such gradients [18,25,28], and we employ a formulation that accounts for the variation of the total emitted dipole power due to the Purcell effect [19]. Sensitivities are obtained at each optimization step after calculating the forward and adjoint electromagnetic fields using

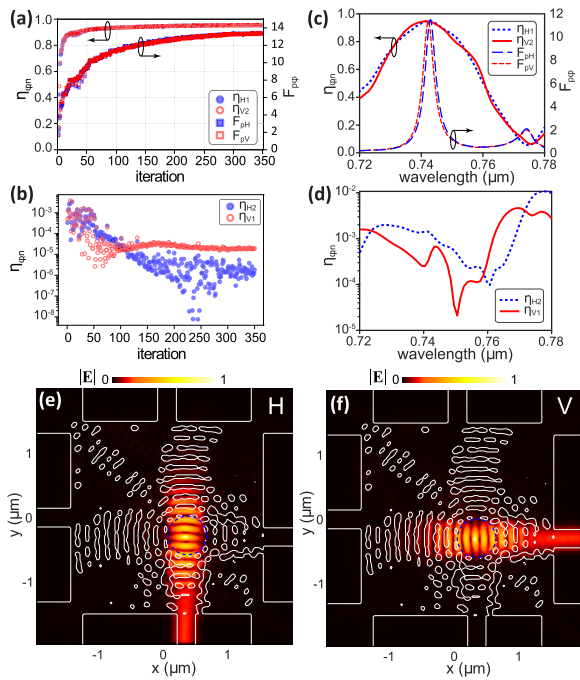


Fig. 2. Evolution of (a) the coupling efficiencies (η_{H1} , η_{V2}) and Purcell factors (F_{pH} , F_{pV}), and (b) the cross talk (η_{H2} , η_{V1}) throughout the optimization process. (c) Optimized coupling efficiencies, Purcell factors, and (d) cross talk as a function of wavelength, simulated by FDTD. (e),(f) Normalized electric field distribution for the final geometry (white lines) considering (e) H- and (f) V-polarized dipoles.

the finite-difference frequency-domain (FDFD) method [29] at a fixed design wavelength.

Following a density-based approach to topology optimization [28], the permittivity at each grid cell inside the design area was assigned to design parameters as $\varepsilon(\tilde{\rho}) = \varepsilon_{\min} + \tilde{\rho}(\varepsilon_{\max} - \varepsilon_{\min})$, $\tilde{\rho} \in [0, 1]$. Here, ε_{\min} and ε_{\max} are the permittivity of vacuum and the bulk semiconductor, respectively, and $\tilde{\rho}$ are obtained by applying a tangent hyperbolic projection filter over ρ to enforce binarization [30]. The smoothness of this filter is controlled by a projection parameter that is increased every five iterations, leading to steeper transitions from $\text{Al}_{0.4}\text{Ga}_{0.6}\text{As}$ to vacuum in the design region. To avoid potential QD spectral broadening due to proximity of etched sidewalls [31], the parameters ρ were constrained to unity inside a circle of radius 300 nm centered at the dipole. In Ref. [19], such constraint had a small impact on the optimized coupling efficiency and Purcell factor.

As shown in Fig. 2(a), after 200 iterations, the coupling efficiencies η_{H1} and η_{V2} achieved a value of approximately 0.95 that remained almost constant while the optimization progressed to obtain a well-defined (i.e., binary) permittivity distribution. Figures 2(c) and 2(d) show results of a finite-difference time-domain (FDTD) simulation of dipole emission in the optimized geometry, performed to verify the operation bandwidth. It is evident that the coupling efficiencies remain above 0.79 (−1 dB), and cross talk below 10^{-3} (−30 dB), over a 20-nm range. The wide bandwidth allows simultaneous high-efficiency extraction of the spectrally distinct XX–X and X–G transitions, which are typically separated by 1 nm to 2 nm in wavelength. The small discrepancies between the peak values of η_{H1} and η_{V2} in Fig. 2(c) and those obtained in the optimization, Fig. 2(a), are likely due

to the differences in geometry discretization between the FDFD and FDTD solvers.

Purcell factors of approximately 11.5 were obtained for both dipole orientations, as shown by the resonances centered at 744 nm in the FDTD spectra in Fig. 2(c). The resonances have full widths at half maximum (FWHM) of approximately 3 nm, which relaxes spectral alignment requirements between cavity and emitter, and allows extraction of multiple spectrally separate transitions [2]. Purcell enhancement of the radiative rate is also critical for achieving high photon indistinguishability, which is important for two-photon interference in photonic quantum information processing [32]. The cross talk remains at or below 10^{-3} within the bandwidth of the resonances, as shown in Fig. 2(d). The bandwidth of the Purcell factor is narrower than that of the coupling efficiency, which would enable choosing a specific ratio of the X and XX Purcell factors while keeping a high coupling efficiency for both. This would be necessary for high indistinguishability in cascaded emission [11].

The optimized geometry, indicated by white lines in Figs. 2(e) and 2(f), is almost symmetric with respect to the diagonal between the x and y axes. A roughly periodic, Bragg reflector-like structure surrounds the protected region marked by the blue dashed lines. The electric field profiles produced by H and V dipoles, plotted in Figs. 2(e) and 2(f), feature cavity mode-like standing-wave patterns, which lead to the Purcell effect. The geometry features complex shapes of small dimensions (<50 nm), which are challenging to fabricate. For improved fabricability, more sophisticated projection filters could be applied [33] or the objective function could include penalties for hard-to-fabricate shapes and sizes [34,35].

An important consideration for any quantum emitter device is the performance robustness with respect to the emitter's position and orientation [36]. Via FDTD simulations, we obtain the coupling efficiencies, cross talk, and Purcell factors considering translations and rotations of the QD relative to the target configuration. The results, in Supplement 1, indicate that position deviations within ± 25 nm are necessary to ensure performance reductions of less than 10%, a typical requirement for small mode volume nanophotonic cavities [36,37].

As the performance of inverse-designed structures is impacted by the initial geometry [19], we investigated device performance for different positions of the QD and output waveguides. The QD was displaced along the diagonal axis shown in Fig. 3(a), and the output waveguides were aligned with the emitter. The same number of optimization iterations as in Figs. 2(a) and 2(b) were performed. Figure 3(b) indicates that the coupling efficiencies and Purcell factors are highest when the QD is displaced toward the waveguides, with greater benefit for the Purcell factors. In contrast, the cross talks in Fig. 3(c) exhibit no obvious trend with QD displacement, remaining less than 3×10^{-4} throughout. This analysis is why the earlier figures have the QD displaced approximately 400 nm from the center of the design region. Qualitatively, such displacement provides more space to improve the reflectivity of the Bragg-like structure generated by the algorithm.

In summary, we performed the inverse design of a nanophotonic geometry that can be used for the creation of an efficient source of waveguide-coupled, path-entangled photon pairs based on single GaAs quantum dots. The optimized geometry has a peak coupling efficiency of 0.95 (−0.22 dB), cross talk below 10^{-3} (−30 dB), and Purcell factor of 11.5 for both perpendicular QD transitions. Wide operating bandwidths are also

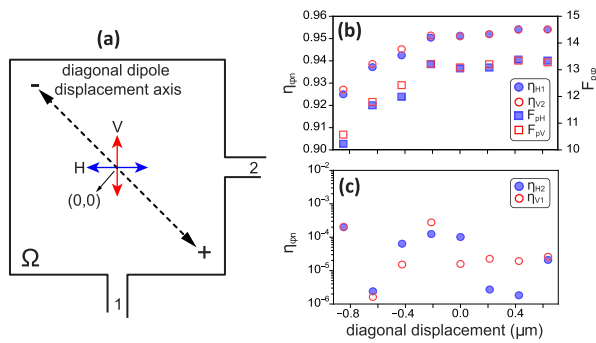


Fig. 3. Optimization results for different positions of the QD within the design region Ω . (a) Schematic showing variation of starting geometry. The QD position is varied along a diagonal line, while the output waveguides are moved so they remain aligned with the QD. (b) Optimized coupling efficiencies and Purcell factors, and (c) cross talks for different QD positions.

predicted (3-nm and 20-nm FWHM for Purcell enhancement and coupling efficiency), which relax requirements for spectral alignment between the QD and the nanostructure. The generated design presents similar challenges regarding performance robustness to QD position and orientation as typical nanophotonic designs [37], which can impact device yield [36]. Overall, our results indicate that with a proper figure-of-merit, the inverse design approach is capable of producing nanophotonic geometries that provide non-trivial interfaces to single quantum emitters, with competitive performance and fabricability compared to conventionally designed devices.

Funding. Sao Paulo Research Foundation (FAPESP) (2021/10249-2); National Science Foundation (OAC-1726534).

Acknowledgments. High-performance computing was performed at the Brazilian National Laboratory of Scientific Computation and the West Virginia University Thorny Flat cluster.

Disclosures. The authors declare no conflicts of interest.

Data availability. Data underlying the results presented in this paper are not publicly available at this time but may be obtained from the authors upon reasonable request.

Supplemental document. See Supplement 1 for supporting content.

REFERENCES

- H. Wang, H. Hu, T.-H. Chung, J. Qin, X. Yang, J.-P. Li, R.-Z. Liu, H.-S. Zhong, Y.-M. He, X. Ding, Y.-H. Deng, Q. Dai, Y.-H. Huo, S. Höfling, C.-Y. Lu, and J.-W. Pan, *Phys. Rev. Lett.* **122**, 113602 (2019).
- J. Liu, R. Su, Y. Wei, B. Yao, S. F. C. d. Silva, Y. Yu, J. Iles-Smith, K. Srinivasan, A. Rastelli, J. Li, and X. Wang, *Nat. Nanotechnol.* **14**, 586 (2019).
- C. Schimpf, M. Reindl, F. Basso Basset, K. D. Jöns, R. Trotta, and A. Rastelli, *Appl. Phys. Lett.* **118**, 100502 (2021).
- N. Somaschi, V. Giesz, L. D. Santis, J. C. Loreda, M. P. Almeida, G. Hornecker, S. L. Portalupi, T. Grange, C. Antón, J. Demory, C. Gómez, I. Sagnes, N. D. Lanzillotti-Kimura, A. Lemaître, A. Auffeves, A. G. White, L. Lanco, and P. Senellart, *Nat. Photonics* **10**, 340 (2016).
- X. Ding, Y. He, Z.-C. Duan, N. Gregersen, M.-C. Chen, S. Unsleber, S. Maier, C. Schneider, M. Kamp, S. Höfling, C.-Y. Lu, and J.-W. Pan, *Phys. Rev. Lett.* **116**, 020401 (2016).
- R. Uppu, F. T. Pedersen, Y. Wang, C. T. Olesen, C. Papon, X. Zhou, L. Midolo, S. Scholz, A. D. Wieck, A. Ludwig, and P. Lodahl, *Sci. Adv.* **6**, eabc8268 (2020).
- O. Benson, C. Santori, M. Pelton, and Y. Yamamoto, *Phys. Rev. Lett.* **84**, 2513 (2000).
- N. Akopian, N. H. Lindner, E. Poem, Y. Berlatzky, J. Avron, D. Gershoni, B. D. Gerardot, and P. M. Petroff, *Phys. Rev. Lett.* **96**, 130501 (2006).
- A. Müller, W. Fang, J. Lawall, and G. S. Solomon, *Phys. Rev. Lett.* **103**, 217402 (2009).
- D. Huber, M. Reindl, Y. Huo, H. Huang, J. S. Wildmann, O. G. Schmidt, A. Rastelli, and R. Trotta, *Nat. Commun.* **8**, 15506 (2017).
- E. Schöll, L. Schweickert, L. Hanschke, K. D. Zeuner, F. Sbresny, T. Lettner, R. Trivedi, M. Reindl, S. F. Covre da Silva, R. Trotta, J. J. Finley, J. Vuckovic, K. Müller, A. Rastelli, V. Zwiller, and K. D. Jöns, *Phys. Rev. Lett.* **125**, 233605 (2020).
- A. Dousse, J. Suffczynski, A. Beveratos, O. Krebs, A. Lemaître, I. Sagnes, J. Bloch, P. Voisin, and P. Senellart, *Nature* **466**, 217 (2010).
- M. A. M. Versteegh, M. E. Reimer, K. D. Jöns, D. Dalacu, P. J. Poole, A. Gulinati, A. Giudice, and V. Zwiller, *Nat. Commun.* **5**, 5298 (2014).
- M. N. Makhonin, J. E. Dixon, R. J. Coles, B. Royall, I. J. Luxmoore, E. Clarke, M. Hugues, M. S. Skolnick, and A. M. Fox, *Nano Lett.* **14**, 6997 (2014).
- P. Schnauber, A. Singh, J. Schall, S. I. Park, J. D. Song, S. Rodt, K. Srinivasan, S. Reitzenstein, and M. Davanco, *Nano Lett.* **19**, 7164 (2019).
- S. Rodt and S. Reitzenstein, *APL Photonics* **6**, 010901 (2021).
- T. Jin, X. Li, R. Liu, W. Ou, Y. Zhu, X. Wang, J. Liu, Y. Huo, X. Ou, and J. Zhang, *Nano Lett.* **22**, 586 (2022).
- C. M. Lalau-Keraly, S. Bhargava, O. D. Miller, and E. Yablonovitch, *Opt. Express* **21**, 21693 (2013).
- E. G. Melo, W. Eshbaugh, E. B. Flagg, and M. Davanco, *ACS Photonics* **10**, 959 (2022).
- M. Bayer, A. Kuther, A. Forchel, A. Gorbunov, V. B. Timofeev, F. Schäfer, J. P. Reithmaier, T. L. Reinecke, and S. N. Walck, *Phys. Rev. Lett.* **82**, 1748 (1999).
- R. M. Stevenson, A. J. Hudson, A. J. Bennett, R. J. Young, C. A. Nicoll, D. A. Ritchie, and A. J. Shields, *Phys. Rev. Lett.* **101**, 170501 (2008).
- A. W. Elshaari, I. E. Zadeh, A. Fognini, M. E. Reimer, D. Dalacu, P. J. Poole, V. Zwiller, and K. D. Jöns, *Nat. Commun.* **8**, 379 (2017).
- R. Trotta, E. Zallo, C. Ortix, P. Atkinson, J. D. Plumhof, J. van den Brink, A. Rastelli, and O. G. Schmidt, *Phys. Rev. Lett.* **109**, 147401 (2012).
- H. Ollivier, P. Priya, A. Harouri, I. Sagnes, A. Lemaître, O. Krebs, L. Lanco, N. Lanzillotti-Kimura, M. Esmann, and P. Senellart, *Phys. Rev. Lett.* **129**, 057401 (2022).
- A. Michaels and E. Yablonovitch, *Opt. Express* **26**, 31717 (2018).
- O. Shapira, A. F. Abouraddy, J. D. Joannopoulos, and Y. Fink, *Phys. Rev. Lett.* **94**, 143902 (2005).
- X. Liang and S. G. Johnson, *Opt. Express* **21**, 30812 (2013).
- J. S. Jensen and O. Sigmund, *Laser Photonics Rev.* **5**, 308 (2011).
- L. Su, D. Vercruyssen, J. Skarda, N. V. Sapra, J. A. Petykiewicz, and J. Vuckovic, *Appl. Phys. Rev.* **7**, 011407 (2020).
- F. Wang, B. S. Lazarov, and O. Sigmund, *Struct. Multidisc. Optim.* **43**, 767 (2011).
- F. Liu, A. J. Brash, J. O'Hara, L. M. P. P. Martins, C. L. Phillips, R. J. Coles, B. Royall, E. Clarke, C. Bentham, N. Prtljaga, I. E. Itskevich, L. R. Wilson, M. S. Skolnick, and A. M. Fox, *Nat. Nanotechnol.* **13**, 835 (2018).
- J. Bylander, I. Robert-Philip, and I. Abram, *Eur. Phys. J. D* **22**, 295 (2003).
- O. Sigmund, *Acta Mech. Sin.* **25**, 227 (2009).
- D. Vercruyssen, N. V. Sapra, L. Su, R. Trivedi, and J. Vuckovic, *Sci. Rep.* **9**, 8999 (2019).
- A. M. Hammond, A. Oskooi, A. Oskooi, S. G. Johnson, and S. E. Ralph, *Opt. Express* **29**, 23916 (2021).
- C. R. Copeland, A. L. Pintar, R. G. Dixon, A. Chanana, K. Srinivasan, D. A. Westly, B. R. Ilic, M. I. Davanco, and S. M. Stavis, "Traceable localization enables accurate integration of quantum emitters and photonic structures with high yield," *arXiv* (2023).
- S. Liu, K. Srinivasan, and J. Liu, *Laser Photonics Rev.* **15**, 2100223 (2021).